Polarization Signatures of Quasi-Periodic Oscillations in Simulated Tilted, Truncated Disks

P. Chris Fragile, Deepika A. Bollimpalli, Jeremy D. Schnittman, and Cesare Harvey

¹ Department of Physics and Astronomy, College of Charleston, 66 George Street, Charleston, SC 29424, USA
² Department of Astronomy, Astrophysics & Space Engineering, Indian Institute of Technology Indore, Simrol, Indore 453552, Madhya Pradesh, India

³NASA Goddard Space Flight Center, 8800 Greenbelt Rd, Greenbelt, MD 20771, USA
 ⁴Department of Physics and Astronomy, College of Charleston, 66 George St, Charleston, SC 29424, USA

ABSTRACT

We utilize the Monte-Carlo radiation transport code, Pandurata, to create images, spectra, polarization maps, and light curves from a set of general relativistic magnetohydrodynamic simulations of tilted, truncated, black hole accretion disks. Truncation can have spectral and polarization signatures all its own; tilt introduces both inclination and azimuthal dependencies into the spectra and polarization; and precession and oscillations of the tilted accretion flow inside the truncation radius (what we posit to be the "corona") introduce time dependencies or periodicity to all of this. We use the ray-traced results from our simulations to evaluate the feasibility of measuring these effects, particularly in the context of current and future X-ray polarization observatories. Such detections could greatly improve our understanding of the geometry of accretion disks and coronae in the hard state, the physics of quasi-periodic oscillations (QPOs), and how system properties evolve as sources approach the hard-to-soft state transition.

Keywords: Accretion (14) — X-ray polarization(1571) — Relativistic disks (1388) — Rotating black holes (1406) — Low-mass x-ray binary stars (939)

1. INTRODUCTION

Black hole X-ray binaries (BHXRBs), also known as microquasars owing to their similarities to active galactic nuclei (AGN), are mostly observed whenever they go into outburst, during which they transit through several different spectral states, as they simultaneously vary in luminosity and spectral hardness, often tracing out a "q" shape in a hardness-intensity diagram (Fender et al. 2004; McClintock & Remillard 2006). The current best models that provide a framework for understanding these outbursts relate the spectral evolution to changes in the mass accretion rate, the geometry of the accretion flow, and the presence or absence of different physical components, e.g., a corona or jet (Esin et al. 1997; Begelman & Armitage 2014).

There are two main contributions to the X-ray spectra of BHXRBs that control their hardness during an outburst – a soft, thermal component (below approximately 3 keV) and a hard, power-law component (extending roughly between 10 - 100 keV). The soft component is attributed to thermal, blackbody-like radiation coming from a relatively cold, optically thick and geometrically thin disk. The power-law component is then

generated by the inverse-Compton scattering of soft seed photons from the disk by a radiatively inefficient cloud of hot electrons, i.e., the "corona." The location and geometry of the corona are still under debate. We favor a truncated-disk geometry with a standard, thin disk truncated outside the last stable orbit, and the corona as a geometrically thick, radiatively inefficient accretion flow filling in the gap (Eardley & Lightman 1975; Esin et al. 1997; Liu et al. 2007).

Closely associated with the spectral state changes are changes in the temporal variability of the light curves. Specifically, many BHXRBs (and other compact accretors) exhibit rapid time variability, often in the form of quasi-periodic oscillations (QPOs). Broadly speaking, the QPOs observed in black hole systems are classified as high- ($\gtrsim 60~\rm{Hz}$) and low-frequency ($\lesssim 30~\rm{Hz}$) (Remillard & McClintock 2006; Belloni 2010). Low-frequency QPOs (LFQPOs) are further classified into type-A, B and C, of which the first two are only observed during intermediate states (Motta 2016). The type-C QPOs are more commonly observed in general (Motta et al. 2012; Motta 2016), being particularly prominent in the hard state. For those QPOs, both the fractional QPO

amplitude and the phase-lag between the hard and soft photons measured at the QPO frequency are found to have inclination dependencies (Motta et al. 2015; van den Eijnden et al. 2017), strongly suggesting a geometric origin (Schnittman et al. 2006a).

A promising model for this QPO is having a finite, inner region of the accretion flow precess as a rigid body (Schnittman et al. 2006a; Ingram et al. 2009). This model can tie in with the truncated disk picture of the hard state if it is the corona that is precessing (Ingram & Done 2011; Fragile et al. 2016). This naturally explains the rise in the QPO frequency during the early phases of the outburst cycle (when the truncation radius is moving inward; Ingram & Done 2011; Fragile et al. 2016; Kubota et al. 2024) and easily reproduces the inclination dependence seen in QPO observations (Veledina et al. 2013). Thus, the time variability and geometry of black hole accretion flows may be closely linked, and polarization measurements may be able to shed light on both.

The Imaging X-ray Polarimetry Explorer (IXPE; Weisskopf et al. 2022) and the X-ray Polarimeter Satellite (XPoSat; Paul 2022) have the ability to detect polarization signatures from accreting compact objects (e.g. Doroshenko et al. 2022; Krawczynski et al. 2022; Podgorný et al. 2023). They can also directly probe the geometries of accretion disks (Schnittman & Krolik 2009; Cheng et al. 2016; Farinelli et al. 2023) and coronae (Schnittman & Krolik 2010; Marinucci et al. 2022; Gianolli et al. 2023). What is new about our work is that we consider the polarization signature of an accretion disk geometry - the truncated disk - that has not been specifically looked at so far, and by using the output of fully general relativistic magnetohydrodynamic (GRMHD) simulations. We also probe the time variability of polarization signatures.

2. METHODS

Our basic approach in this paper is to take a pair of numerical simulations of truncated disks, one tilted and one untilted, plus a simulation of an isolated, tilted torus, all performed using the Cosmos++ GRMHD code (Anninos et al. 2005; Fragile et al. 2012, 2014), and pass them to the fully relativistic, polarization-capable, Monte Carlo radiation transport code, Pandurata (Schnittman & Krolik 2013). This allows us to create light curves, spectra, and polarization maps analogous to what would be observed by IXPE, XPoSat, and future polarization missions. In this section, we provide more details about the simulations themselves and our use of Pandurata.

2.1. Truncated Disk Simulations

We consider three, fully 3D GRMHD simulations of accretion disks. These include the a9b0L4 and a9b15L4 simulations from Bollimpalli et al. (2024) and the isolated, tilted torus simulation from Appendix A of that same paper. The first two simulations differ in terms of the initial alignment of angular momentum axes between the disk and the black hole (with dimensionless spin parameter $a_* = a/M = 0.9$ in both cases). In simulation a9b0L4, the axes are aligned, while in the a9b15L4 and isolated torus simulations, the initial disk angular momentum vectors are oriented along the z-axis, while the black hole spin axis is tilted by an angle $\beta_0 = 15^{\circ}$ toward the -x-axis.

All three simulations are initialized with a finite torus having an inner edge at $6.5\,r_g$ and pressure maximum at $9\,r_g$, where $r_g\equiv GM/c^2$. In the a9b0L4 and a9b15L4 simulations, this torus is surrounded by a thin slab of gas with a constant height of $H=0.4\,r_g$, extending from $15\,r_g$ to the outer boundary of the simulation domain at approximately $250\,r_g$. To preserve the desired thin structure of the outer disk, we implement an artificial cooling function, which is applied exclusively to radii beyond $15\,r_g$.

Both the torus and the slab are threaded with numerous small poloidal loops of magnetic field with alternating polarity. This magnetic field configuration impedes the accumulation of strong net flux in the inner regions, thus precluding the formation of a magnetically arrested disk (MAD).

The simulations are performed in modified Kerr-Schild, spherical-polar coordinates, enabling the placement of the inner domain boundary inside the black hole event horizon. The grid is logarithmically spaced in r, covering the range $r \in [1.4 r_g, 40^{1.5} r_g]$, and uniformly spaced in ϕ , encompassing the entire $[0, 2\pi]$ domain. The polar angle θ is uniformly spaced in the coordinate x_2 , with the grid spacing defined as

$$\theta = \pi x_2 + \frac{1 - h}{2} \sin(2\pi x_2) , \qquad (1)$$

where h=0.5 is used to concentrate grid cells close to the midplane (McKinney 2006). To avoid computing metric terms at the poles, a small cone of opening angle $10^{-15}\pi$ is excised.

All simulations have a base resolution of $48 \times 32 \times 32$, accompanied by three additional levels of static mesh refinement. Adjacent refinement levels differ in resolution by a factor of 2 in each dimension, resulting in a fiducial resolution of $384 \times 256 \times 256$ for most of the grid. The initial two levels of refinement are utilized to adequately resolve both the torus and the thin slab. The third refinement layer enhances the resolution of the thin disk over the range $r \in [10.5 \, r_g, 60 \, r_g]$. See Fig.

1 of Bollimpalli et al. (2024) for the arrangement of the grid and the initial gas distribution.

Once the simulations are initialized, the initial magnetic fields trigger the magneto-rotational instability, leading to turbulence that facilitates the transport of angular momentum and enables accretion. The energy generated in this process causes the torus to inflate, resulting in the formation of a hot and thick flow in the inner regions. The cooling function employed in the thin slab region $(r \geq 15\,r_g)$ acts as a heat sink and helps to regulate the thickness of the disk at the target value of $H/r \approx 0.05$. The simulations have been run for $25,000\,t_g$, where $t_g \equiv GM/c^3$.

The results of these simulations are fully described in Bollimpalli et al. (2023, 2024). The most relevant findings for our current purposes are: 1) that there is a clear signature of solid-body precession of the inner torus when it is tilted, while there is no precession in the outer, thin disk (once the initial bending wave passes by a given radius); and 2) that the tilted simulations also exhibit high-frequency oscillations. Our goal in this paper is to determine whether signatures of tilted, truncated disks and QPOs might be observable in polarized light by IXPE or XPoSat.

2.2. Pandurata

We use the Monte-Carlo radiation transport code Pandurata (Schnittman & Krolik 2013) to post-process our numerical simulations and create images, lightcurves, spectra, and polarization maps analogous to X-ray polarization observations.

Pandurata accepts tabulated simulation or model data, including extrinsic fluid variables such as density, temperature, magnetic field, and the fluid four-velocity at each point in a three-dimensional volume. By ingesting multiple data slices (in the time coordinate), Pandurata can also accommodate studies of variability. Because Pandurata assumes a uniform, sphericalpolar grid in Boyer-Lindquist coordinates (with the exception that it accepts a logarithmic radial coordinate), one of the first steps in our case is to remap the simulation data onto a new grid. To preserve as much of the original simulation data as possible, we map onto a $384 \times 256 \times 256$ grid (uniform in θ and ϕ) with the same inner and outer radial boundaries as the original simulation domain. However, since the Boyer-Lindquist radial coordinate cannot penetrate inside the event horizon, unlike the Kerr-Schild radial coordinate, this means that we have to ignore the first few radial shells of data. This will not effect our results, though, since no photons starting from inside the event horizon can impact observations made at infinity.

The first step in analyzing the simulation data is to convert from "code" to cgs units. We do so by specifying a black hole mass $(10M_{\odot}$ in this case) and Eddington-scaled accretion rate (chosen to be $\dot{M}\approx 0.1L_{\rm Edd}/c^2$), as in Schnittman & Krolik (2013). After reading in and remapping the simulation data, the next step is to locate the photosphere of the disk. We do this by integrating the quantity $\kappa\rho$ starting from the pole of the grid and proceeding toward the midplane following a constant coordinate radius r and azimuth ϕ until $\tau=2$, where

$$\tau_{<}(\theta) = -\int_{\pi}^{\theta} u^{t} \kappa \rho \sqrt{g_{\theta\theta}} d\theta ,$$

$$\tau_{>}(\theta) = \int_{0}^{\theta} u^{t} \kappa \rho \sqrt{g_{\theta\theta}} d\theta ,$$
(2)

and $\kappa=0.4~{\rm cm^2~g^{-1}}$ is the scattering opacity. The functions $\tau_<(\theta)$ and $\tau_>(\theta)$ can be thought of as the optical depth to escape from the bottom or top of the disk, respectively. Figure 1 shows the photosphere for one azimuth near the end of our untilted and tilted simulations. Interestingly, even though we are treating the hot, thick, inner torus region as a proxy for the corona, it is dense enough in our simulations to be optically thick (exist beneath the photosphere).

All the Cosmos++ simulations use a $\Gamma=5/3$ polytrope equation of state, corresponding to a non-relativistic ideal gas-like fluid. This is most appropriate for the coronal regions, where we can directly relate the code temperature to the electron temperature. For the optically thick disk, we instead interpret the code pressure P as representing a radiation-pressure-dominated fluid with

$$T_{\rm rad} = \left(\frac{3c}{4\sigma}P\right)^{1/4},\tag{3}$$

and then using this temperature for the thermal seed spectrum $T_{\rm eff} = T_{\rm rad}$. This same procedure was used in the very first demonstration of the ray tracing of a GRMHD simulation (Schnittman et al. 2006b).

Starting from the photosphere at each radius and azimuth, Pandurata launches $\sim 10^4$ packets of thermal photons into the optically thin regions surrounding the disk¹. The initial direction of a photon packet is selected from an isotropic distribution in the emitting fluid frame, limited by the photosphere surface. Each packet is weighted by a number of geometric emission factors, such that a photon packet emitted from a small patch of optically thick, scattering-dominated accretion disk

 $^{^1}$ To test convergence, we redid a couple of our Pandurata runs using four times as many photon packets. Those results agreed to within 10% or less of the original.

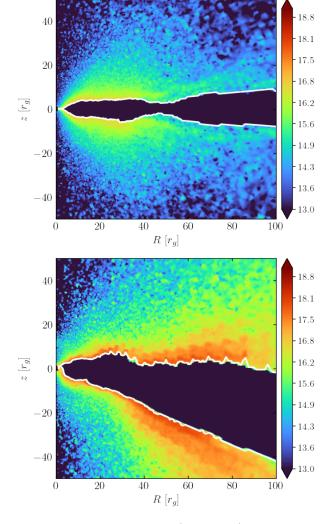


Figure 1. Typical photosphere (white lines) for our untilted (a9b0L4; top panel) and tilted (a9b15L4; bottom panel) simulations at $t = 24,000 t_g$, sliced at $\phi = 0^{\circ}$. Underneath are pseudocolor plots of the local power density due to inverse Compton scattering events in units of erg s⁻¹ cm⁻³.

would have a spectrum of

$$F_{\nu}^{\text{em}} = \frac{1}{f^4} B_{\nu} (f T_{\text{eff}}) \frac{1}{u^t} f_{\text{limb}}(\theta_{\text{em}}) \cos \theta_{\text{em}} dA d\Omega , \quad (4)$$

where F_{ν} has units of spectral luminosity [erg s⁻¹ Hz⁻¹], f is a hardening factor (we use 1.8), B_{ν} is the usual blackbody function, $T_{\rm eff}$ is the effective local temperature, $\cos\theta_{\rm em}$ is a geometric factor, $f_{\rm limb}$ treats the limb darkening (Chandrasekhar 1960), dA is the proper area of the emission region, $d\Omega$ is the solid angle, and $1/u^t = d\tau/dt$ converts from time in the emission frame to that of the coordinate frame. For $T_{\rm eff}(r,\phi)$, we take an average of the radiation temperature from the top and bottom of the photosphere, assuming the gas and radiation are in pressure equilibrium.

The photon packets then follow null geodesics, using the same integrator as described in Schnittman & Bertschinger (2004). Because the geodesic trajectories are independent of photon energy, we simultaneously track photons covering energies in the range $[10^{-3}-10^4]$ keV. However, we do still need to account for Doppler and gravitational redshifting. To do so, we track each photon packet's frequency (or energy) in both the "emitter" and "observer" frames. For a photon packet emitted in a frame with fluid four-velocity $u^{\mu}(em)$ and photon four-momentum $k_{\mu}(em)$ and observed in a frame with $u^{\nu}(obs)$ and $k_{\nu}(obs)$, the redshifted frequency is

$$\nu(\text{obs}) = \nu(\text{em}) \frac{u^{\nu}(\text{obs})k_{\nu}(\text{obs})}{u^{\mu}(\text{em})k_{\mu}(\text{em})} . \tag{5}$$

Whenever a photon packet scatters off the disk or an electron in the corona, the frequencies ν_i are updated and the old observed frame becomes the new emitted frame.

Our main interest is in the polarization of the radiation. Starting from the disk photosphere (assumed to be a scattering-dominated surface), each photon packet is created with a certain polarization according to its emitted direction $\theta_{\rm em}$ (Chandrasekhar 1960). The initial values of the polarization degree range from $\delta = [0-0.12]$ for $\theta_{\rm em} = [0-90^{\circ}]$.

To track the polarization along the geodesic path, we take advantage of the fact that the polarization vector \mathbf{f} is a space-like vector normal to the photon wave vector \mathbf{k} . Therefore, it is constrained by $\mathbf{f} \cdot \mathbf{f} = 1$ and $\mathbf{f} \cdot \mathbf{k} = 0$ (Connors et al. 1980). Since \mathbf{k} is a null vector, we can always redefine \mathbf{f} by adding some multiple of \mathbf{k} to it and thus write the polarization vector as

$$f^{\mu} = [0, \cos \psi e_1^i + \sin \psi e_2^i] \tag{6}$$

for some space-like basis vectors \mathbf{e}_1 and \mathbf{e}_2 normal to \mathbf{k} . In this basis, we can write

$$X = Q/I = \delta \cos 2\psi ,$$

$$Y = U/I = \delta \sin 2\psi ,$$
 (7)

where I, Q, and U are the classical Stokes parameters and ψ is the polarization angle. The polarization degree δ is invariant along the geodesic path.

Once the photon packets have finally escaped the simulation domain on their way to an observer, they are collected into $\{\theta,\phi\}$ bins. We use 41 evenly spaced bins in the θ -direction and 8 in the ϕ -direction². When a photon packet reaches "infinity", or in our case a spherical

 $^{^2}$ For some of the untilted simulation results, we collect all of the photon packets into a single azimuthal bin, as appropriate in the case of axisymmetry.

shell with $R_{\rm shell}=10000\,r_g$, the detector coordinates are defined such that the +x axis is along the $+\phi$ direction and the +y axis is in the $-\theta$ direction. This corresponds to horizontal polarization having $\psi=0^\circ$ or 180° , and vertical polarization characterized by $\psi=\pm90^\circ$. Furthermore, for these calculations, we employ the "fast light" approximation which does not account for light travel time across the simulation volume. This is appropriate for simulations where the data is stored and analyzed with relatively coarse temporal sampling.

3. RESULTS

We present our results first for the untilted case (a9b0L4) before turning to the tilted ones. We look at light curves, spectra, images, and polarization measures.

3.1. Untilted, Truncated Disk

Because the untilted disk is largely axisymmetric (particularly in a time-averaged sense), we do not expect its observational characteristics to depend strongly on the observer azimuth. Therefore, in this section, we collect all the photon packets into a single azimuthal bin. This will not be the case in the sections on tilted disks.

Since the azimuthal angle is not a factor in this section, we focus instead on the inclination-dependence of our results. We adopt the usual convention, with $i = 0^{\circ}$ being a view straight down the black hole spin axis (faceon to the disk) and $i = 90^{\circ}$ being an observer in the plane of the disk (edge-on). Comparing a nearly face-on view with an edge-on one, we would expect the face-on one to have a higher overall flux (since it experiences less limb darkening), yet a lower amount of polarization (since photon packets leaving normal to the disk surface start with zero polarization and have a shorter path through the corona, thus reducing their likelihood of scattering). This is confirmed in Figure 2, where we plot flux and polarization spectra for observer inclinations of $i = 18, 45, \text{ and } 72^{\circ}$. The nearly face-on disk $(i = 18^{\circ})$ is approximately 10 times brighter across much of the spectrum than the nearly edge-on case $(i = 72^{\circ})$, but only has a polarization degree of < 2%, whereas the nearly edge-on case has a polarization of $\geq 5\%$, except at high energies. In all cases, the polarization angle is close to 0° for $E \lesssim 10 \text{ keV}$, as expected for emission from a planar disk with its symmetry axis pointed vertically (Schnittman & Krolik 2009).

By comparing the total intensity and polarization images of the nearly face-on and edge-on cases as depicted in Figure 3, we can easily understand the results of Figure 2. For the nearly edge-on image (bottom panel), there is a high degree of scattering-induced limb darkening of the original photon packets (Chandrasekhar

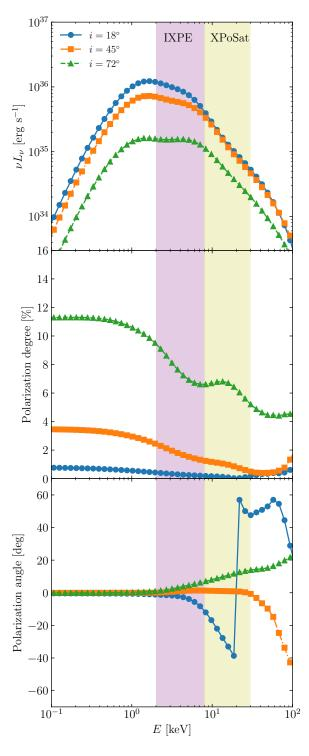


Figure 2. Flux (top panel), polarization degree (middle panel), and polarization angle (bottom panel) at $t=24,000\,t_g$ plotted as a function of energy for three different observer inclinations for our untilted, truncated disk simulation (a9b0L4). Lower inclinations show higher flux, but lower polarization degrees. Our results span the IXPE and XPoSat sensitivity ranges.

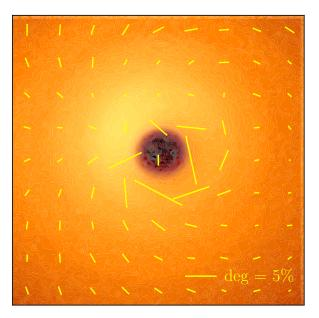
1960). Additionally, most of the photon packets must traverse a lengthy path through the corona, so are more likely to be scattered out of the observer's line of sight or otherwise attenuated. By contrast, for the nearly face-on view (top panel), most of the photon packets start with relatively little limb darkening and travel a shorter path through the corona to the observer. This explains why the top image has a higher overall intensity. However, since photons launched perpendicular to the disk are created with very low polarization fractions, the top (nearly face-on) image shows mostly short polarization vectors, except close to the black hole where lightbending effects amplify the polarization. The nearly edge-on image, by contrast, shows much longer, mostly horizontal, polarization vectors, consistent with the fact that most of these photon packets were launched nearly parallel to the disk surface and had a higher likelihood of scattering within the disk (Chandrasekhar 1960).

3.1.1. Spectral Components

One of the powerful things we can do with a raytracing code like Pandurata is track each photon packet's history from creation in the photosphere to its collection at the camera. We can then use this information to break the flux and polarization spectra down according to the history of the different photon packets, as we do in Figures 4 and 5. In this paper, we track "Disk" photons that originate in the photosphere and escape to the observer without scattering, photons that scatter once off the disk ("Disk Scatter", also called returning radiation), photons that scatter once in the corona ("Corona Scatter"), and photons that scatter once off the disk and once in the corona ("Disk & Corona"). When working with the Stokes parameters (see equations 7), we can simply add the frequency-dependent I_{ν} , Q_{ν} , and U_{ν} from all the relevant photon packets to get the total spectrum and polarization signal, as given in Figure 2 and depicted in Figure 4 as solid black lines.

In Figure 4 (the nearly face-on case), we see that the disk contribution dominates the flux spectrum (top panel) to slightly past the thermal cutoff ($\sim 5~\rm keV$), beyond which the corona scatter and disk & corona components contribute roughly equally to the power-law tail. Not surprisingly then, in the polarization measures, the disk component factors most heavily up to that same cutoff, beyond which, the corona scatter photons begin to have a greater influence on the polarization. (The disk & corona component always has a very small polarization degree, close to 0.)

For the nearly edge-on case in Figure 5, the situation is very different. The corona scatter photons dominate the flux spectrum over the entire energy range. Thus,



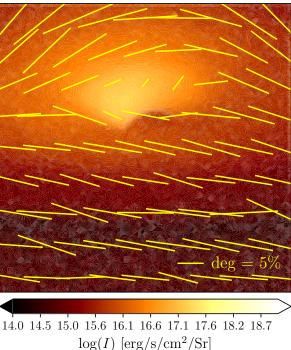


Figure 3. Total intensity images with polarization vectors overlaid for low ($i=18^{\circ}$, top panel) and high ($i=72^{\circ}$, bottom panel) inclinations. Both images represent $40r_g \times 40r_g$ fields of view centered on the black hole.

they also largely dominate the polarization measures, although the disk photons keep the polarization from being as high as it might otherwise be at low energies ($\lesssim 1 \text{ keV}$). In both cases we see that the disk scatter component is characterized by a nearly vertical polarization angle ($\pm 90^{\circ}$), due to the large-angle scattering

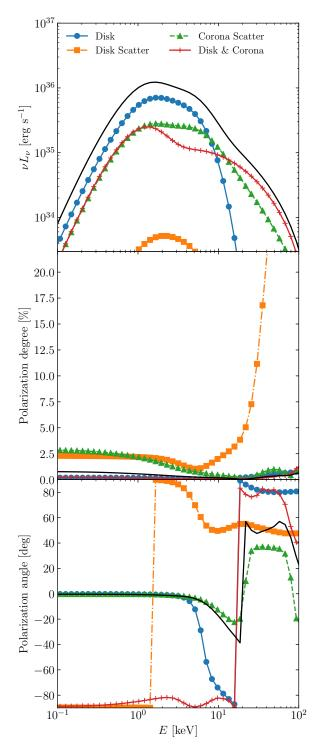


Figure 4. Flux (top panel), polarization degree (middle panel), and polarization angle (bottom panel) as a function of energy for a nearly face-on observer ($i=18^{\circ}$) broken down by the history of the photon packets. These data are for the untilted, truncated disk simulation (a9b0L4) at $t=24,000\,t_g$. "Disk" photons are created at the photosphere, "Disk Scatter" photons scatter once off the disk, "Corona Scatter" photons scatter once in the corona, and "Disk & Corona" photons scatter once each off the disk and corona. The solid black line in each panel gives the total value when all the components are properly weighted.

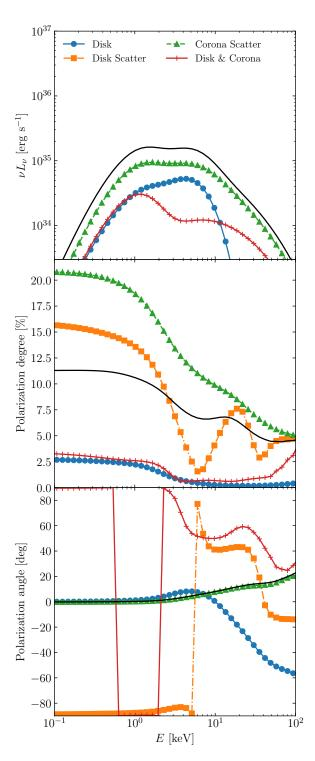


Figure 5. Same as Fig. 4, except for a nearly edge-on observer $(i=72^{\circ})$.

experience by returning radiation (Schnittman & Krolik 2009).

3.1.2. Time Dependence

Lastly, we look at how the flux and polarization measures vary as a function of time for the untilted case (Figure 6). We find that, after some initial period of adjustment lasting $\lesssim 20,000\,t_g$, all of the measures reach nearly steady values (dependent only on inclination). This is consistent with the lack of time variability seen in this simulation's hydrodynamic variables (Bollimpalli et al. 2023, 2024). The different sensitivity ranges of IXPE (2-8 keV) and XPoSat (8-30 keV) explain why the curves look different for those two instruments even at the same inclination.

3.2. Tilted, Truncated Disk

Our ultimate goal in this work is to demonstrate that QPOs are observable through their time-varying polarization signatures. We consider both a low-frequency QPO attributed to the precession of a tilted, thick-disk component and higher frequency QPOs that show up spontaneously in our tilted simulations. For our tilted, truncated disk simulation (a9b15L4), we focus on the part of the simulation that covers the first quarter of a precession period (about $25,000\,t_g$). Unfortunately, it is difficult in this limited period to discern the effects of precession in the polarization light curves, owing to confusion with the initial transient period of the simulation, which lasts almost $20,000\,t_g$, as seen for the untilted case (Figure 6).

Therefore, rather than looking for the time variability due to precession in the light curves of a fixed observer, we instead focus on observations at a single time, but from different azimuths (moving the camera to simulate precession). In order to properly capture the effect of the inner region precessing, it is important to keep the observer inclination fixed with respect to the symmetry axis of the *outer* disk (as nearly as possible given our finite binning). In this section, we keep that inclination at $i = 72^{\circ}$. Note that this means we are changing the inclination of the observer with respect to the black hole spin axis and symmetry axis of the inner torus, which is why we expect the polarization signature to vary. In the next section (3.3), we present results of a simulation where we follow an isolated torus for more than a full precession cycle and can therefore focus on a light curve from a single observer azimuth.

Before considering the azimuthal dependence of the polarization measures, we first comment on the overall flux from our tilted, truncated disk (Figure 7, top panel). Comparing with the $i=72^{\circ}$ curve in Figure 2, we see that the peak flux in the tilted case is higher for most azimuths, and also that the spectrum is harder (peaks at higher energies). This may be partly due to extra dissipation associated with tilted disks (Fragile & Blaes

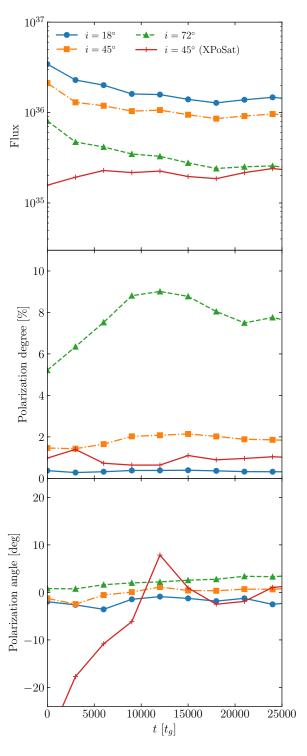


Figure 6. Flux (top panel), polarization degree (middle panel), and polarization angle (bottom panel) plotted as a function of time for three different observer inclinations integrated over the IXPE sensitivity range and one inclination for XPoSat for our untilted simulation (a9b0L4). After a transient period ($\lesssim 20,000\,t_g$), all of the measures settle into roughly constant values.

2008; Generozov et al. 2014), but is mostly attributed to the much greater coronal power in the tilted case (compare the top and bottom panels of Figure 1).

More interestingly, there is a clear azimuthal dependence to the flux, especially above 1 keV, indicating that this QPO could be detected in both the IXPE and XPoSat bands. The polarization signatures (middle and bottom panels of Figure 7) also vary greatly with azimuth. The polarization degree appears about equally variable in both the IXPE and XPoSat bands, whereas the polarization angle is definitely more variable in the XPoSat band, swinging from about 50° for the $\phi = 315 - 360^{\circ}$ bin to -70° for the $45 - 90^{\circ}$ bin. The polarization angle can even have different signs for the same azimuth depending on the energy band (e.g., the blue and orange curves). Similar energy dependence of the polarization angle has been observed for at least one active galactic nucleus source (Gianolli et al. 2024), although entirely within the IXPE band and with the polarization degree rising, rather than falling, with energy. These results demonstrate the potential of polarization to diagnose tilted disks and precession. We would expect the variability over one precession cycle to be similar to that exhibited in Figure 7, which we confirm for an isolated, tilted torus in Section 3.3.

3.2.1. Spectral Components

To better understand the results of Figure 7, we can break down the observations into their spectral components as we did in Figure 4. We focus, in Figure 8, on the $\phi = 45 - 90^{\circ}$ azimuthal bin. We find that the disk component almost matches the corona scattering up to almost 10 keV, beyond which the corona scatter and disk & corona components dominate, somewhat similar to Figure 4. Accordingly, these same three components control the polarization measures. Here, however, is where the differences from the untilted case become most apparent. The degree and angle of polarization show interesting variations with energy right through the sensitivity ranges of IXPE and XPoSat. These variations are driven mainly by changes in the corona scatter contribution, which is the component that should be most sensitive to tilt.

3.2.2. High-frequency QPO

One of the most remarkable results of our tilted, truncated disk simulations is that, along with the precession of the inner torus, they also spontaneously develop high-frequency QPOs (Bollimpalli et al. 2024). In terms of hydrodynamic variables, these QPOs are most apparent in the vertical velocity component of the gas, as it seems the presence of tilt excites vertical oscillations of the inner torus. For the a9b15L4 simulation, this QPO has a

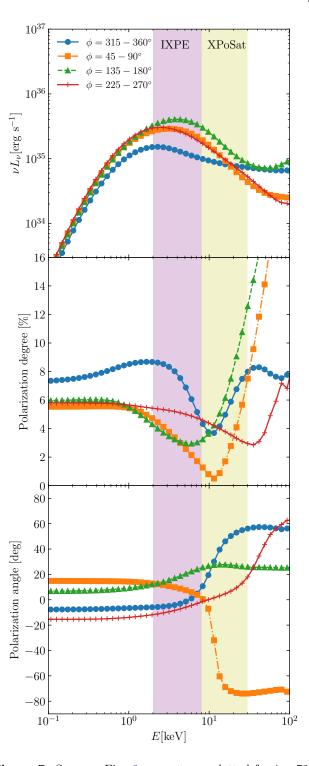


Figure 7. Same as Fig. 2, except now plotted for $i=72^{\circ}$ in four different azimuthal bins for our tilted, truncated disk simulation (a9b15L4). Note the strong dependence of polarization on observer azimuth in both the IXPE and XPoSat bands.

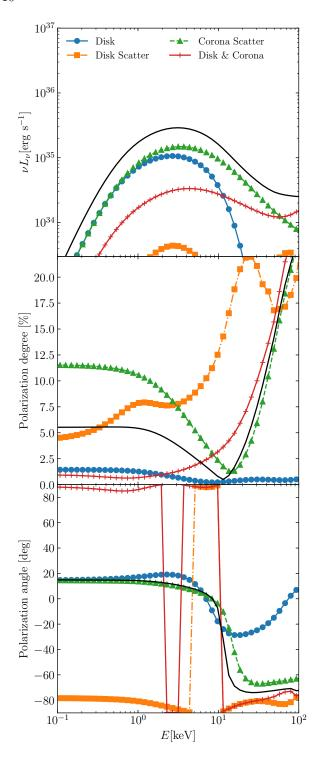


Figure 8. Same as Fig. 5, except for our tilted, truncated disk simulation (a9b15L4) in the $45^{\circ} < \phi \le 90^{\circ}$ bin.

period of approximately 500 t_g (approximately 40 Hz for a $10 M_{\odot}$ black hole), which can be seen in Figure 9 (middle panel) where we plot the time evolution of the disk's mid-plane angle, $\theta_{\rm mid}$, measured at a fixed azimuthal

angle near the inner edge of the disk. The period of oscillations in that curve closely match the period of oscillations seen in the polarization light curves covering the same simulation time, especially in the higher-energy XPoSat band.

3.3. Isolated, Tilted Torus

The last simulation we consider is of an isolated, tilted torus. We include this case because it is the only one of our simulations that evolved for a full precession period. Thus, we can create a complete map between the polarization measures and precession phase. This is done in Figure 10, where, like Figure 6, we plot the flux, polarization degree, and polarization angle as a function of time. However, unlike Figure 6 where the lines are basically flat after some initial period of adjustment, we see prominent fluctuations in the polarization measures. The polarization angle, in particular, clearly traces the two precession periods of the simulation for all observer inclinations and energy ranges. The polarization degree is less well synchronized with the precession, though the intermediate inclination ($i = 45^{\circ}$) does show roughly two periods of oscillation, though with evidence for a possible higher-frequency oscillation added on top of the

Indeed, if we focus on a higher-time-resolution interval, as in Figure 11, then we clearly see another QPO, this one with a period of $\sim 200 t_q$. This is interesting, as no high-frequency QPO was previously reported for this simulation. This may be because Bollimpalli et al. (2024) focused primarily on radial and vertical oscillation modes, whereas this QPO seems to be associated with the orbital modulation of an m=1, nonaxisymmetric mode that arises from the Papaloizou-Pringle instability (PPI; Papaloizou & Pringle 1984). This particular high-frequency QPO may not be a realistic mode for a full accretion disk, as the PPI applies most strongly to small, isolated tori, but that is not really the point. The point is that we have demonstrated that polarization measures are sensitive to QPOs with a variety of frequencies and modes.

4. DISCUSSION

4.1. Comparison to Previous Work

This is not the first time Pandurata has been used to post-process the results of numerical simulations, though it is the first time it has been applied to truncated and tilted disks. GRMHD simulations are particularly well-suited for making polarization predictions because polarization is fundamentally a measurement of geometry. Even when the simulations do not include a complete treatment of the gas thermodynamics and ra-

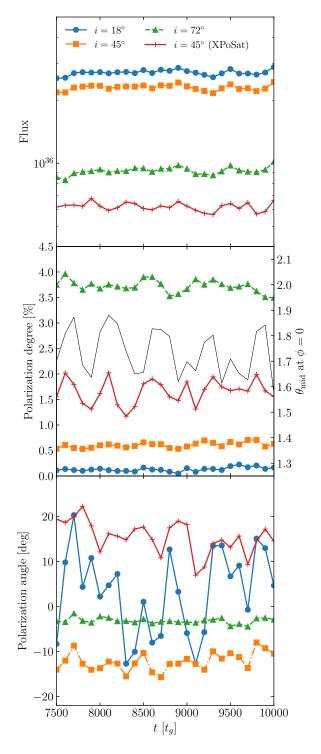


Figure 9. Same as Fig. 6, except for a short segment of our tilted, truncated disk simulation (a9b15L4) in the $315^{\circ} < \phi \leq 360^{\circ}$ bin. The middle panel also includes the time evolution of the disk's mid-plane angle, $\theta_{\rm mid}$, measured at a fixed azimuth, $\phi=0$, for $r=5\,r_g$ (solid, black), showing the vertical oscillations of the inner torus.

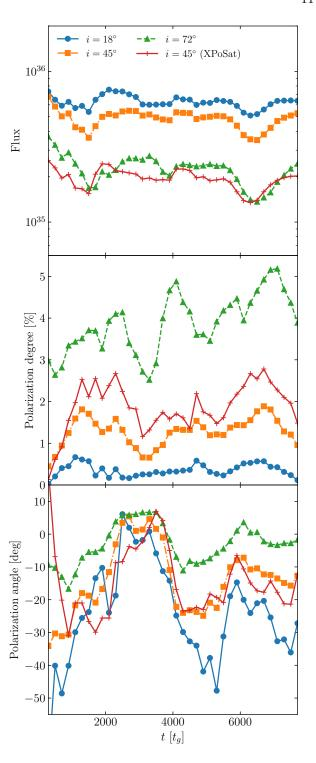


Figure 10. Same as Fig. 6, except for the isolated, tilted torus and only including photon packets arriving in the $315^{\circ} < \phi \leq 360^{\circ}$ azimuthal bin. This plot covers roughly two full precession periods, which are easily seen in the polarization angle for all inclinations and energy bands.

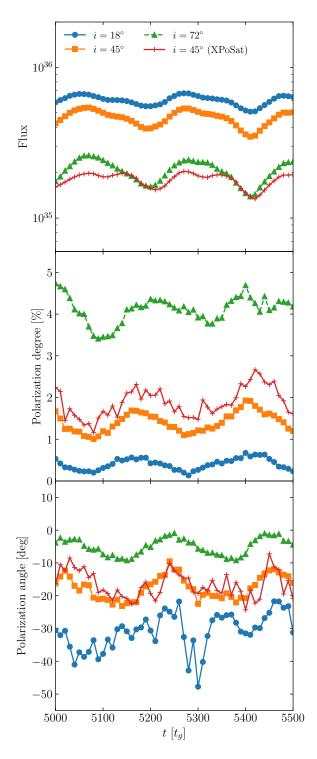


Figure 11. Same as Fig. 10, except zoomed in on the period from 5,000 to $5,500 t_g$, showing evidence for a high-frequency QPO with a period of approximately $200 t_g$.

diation transport, they still provide a relatively reliable picture of the bulk features of the accretion flow. Along with Pandurata's post-processing capabilities, we can also gain valuable insight into the energy-dependent polarization features that come from electron scattering in the corona.

Broadly speaking, our results show similarities to previous studies (e.g., Schnittman & Krolik 2009), especially in cases where the disk component dominates the flux (i.e., our untilted, nearly face-on results). In those cases, the spectrum is consistent with a multitemperature blackbody that is well modeled by Novikov & Thorne (1973). The polarization degree is modest (only a few percent), and the polarization angle is close to zero (i.e., horizontal). When including the returning radiation, we expect a transition from horizontal to vertical polarization just beyond the thermal peak, as the large scattering angles (and thus high degree of vertical polarization) of the deflected disk photons begin to dominate the polarization signal. As described in Schnittman & Krolik (2009), this transition occurs at lower energies for lower inclinations, as the direct disk contribution is inherently less polarized, so easier to "overcome" by the scattered disk contribution.

Thus, we can interpret many of our results in terms of a standard, thermal disk with a time-varying inclination. At a given energy above the thermal peak, even relatively small fluctuations in the inclination can lead to large swings in the polarization angle and degree, essentially serving as a magnifying glass to amplify the observability of the QPOs.

For higher inclination (more edge-on) cases, where the corona scattering component becomes more prominent, our results differ from most previous studies. In those cases, we find generally harder spectra and much larger polarization degrees ($\gtrsim 5\%$).

4.2. Prospects for Detection

In this work, we have shown that various QPO mechanisms, including global precession of a tilted torus, orbital modulation by a non-axisymmetric mode, and vertical oscillations in a tilted, truncated disk, can all produce notable changes in polarization. Our hope is that these polarization modulations may be detectable with a dedicated X-ray polarimeter, such as IXPE (Weisskopf et al. 2022) or XPoSat (Paul 2022). However, we must acknowledge that this would be a very challenging measurement to make in practice. The main difficulty has to do with timescales. Even the low-frequency, type-C QPO has frequencies in the range of 0.1-10 Hz, while polarization measurements typically require long exposure times (tens or hundreds of kiloseconds for IXPE).

This is obviously many orders of magnitude longer than the QPO period.

The best hope for detection is to "phase fold" the polarization measurements with the QPO signal (Ingram et al. 2015). Since IXPE carefully tracks the arrival time of each photon, it is possible, in principle, to correlate each of the photons with the appropriate QPO phase and in this way bin the photons to build up a detectable signal. A similar technique has been used to correlate energy shifts in spectral reflection features with QPO phase (Miller & Homan 2005; Schnittman et al. 2006a; Ingram et al. 2016). Adding to the challenge for polarization is the fact that QPOs often change frequency on timescales comparable to a typical IXPE exposure, so one has to account for this drift when correlating arrival times. On top of that, the QPO frequency may be tied to the location of the truncation radius. As the truncation radius moves inward and the QPO frequency rises, the strength of the polarization signal will likely change, further complicating detection. Still, the prospect of demonstrating a correlation between polarization and QPO phase and thereby potentially confirming the correct models for various QPOs demands that such measurements be attempted.

An additional complication not considered here is the possibility of Faraday rotation of the polarization as it passes through the corona. If the magnetic field is relatively disordered, then any Faraday rotation would tend to wash out the polarization degree through random fluctuations. Since early IXPE observations of BHXRBs have, if anything, shown surprisingly high values of polarization, this suggests that dilution due to Faraday rotation at X-ray energies must be relatively small. Barnier & Done (2024) suggest this lack of Faraday rotation can be used to put meaningful upper limits on the magnetic field strengths in these systems.

5. CONCLUSION

We have post-processed the untilted and tilted, truncated black hole accretion disk and isolated, tilted torus simulations of Bollimpalli et al. (2024) using the polarization-capable, Monte-Carlo radiation transport code Pandurata (Schnittman & Krolik 2013). Our results show reasonable agreement with previous work in that, whenever the disk component dominates, we find a roughly thermal spectrum with an emission peak at a few keV, appropriate for a black hole with $a_{\ast}=0.9$, disk images that appear nearly symmetric, and polarization degrees that are generally low.

As the disks are viewed more edge on, the spectra become dimmer (due to limb darkening) and harder (due to more coronal scattering). Disk images become less symmetric, as Doppler boosting enhances the approaching side relative to the receding one. The polarization degree also increases due both to properties of the seed photons in a scattering-dominated disk atmosphere (Chandrasekhar 1960) and additional inverse Compton scattering in the corona (Schnittman & Krolik 2010).

For our untilted, truncated disk, we find very little azimuthal or time dependence, as expected, though we do find a strong inclination dependence. For a nearly edge-on observation, the spectrum can be quite hard, with coronal scattering dominating at all energies. The polarization degree can also be large ($\gtrsim 5\%$) in such cases.

Based on our tilted, truncated disk, we can confirm that global precession of a hot, inner flow produces detectable changes in the polarization. The polarization degree can vary by a few percent over a precession cycle, and the polarization angle can change by 90° or more. We even showed what this variability could look like over a full QPO phase for the case of an isolated, tilted torus.

We also clearly identified high-frequency QPOs in both of our tilted simulations, even though the QPOs are attributed to different mechanisms. This means polarimetry might one day be used to shed light on lowand high-frequency QPOs alike.

Finally, although, we have only tested one black hole spin $(a_* = 0.9)$, one tilt $(\beta = 15^{\circ})$, and one truncation radius $(r_{\rm Tr} = 15\,r_g)$, we hope our results will motivate future observations by IXPE, XPoSat, and other X-ray polarization experiments. In the meantime, we also plan to expand the parameter space of this study by considering other spins, tilts, and disk geometries.

We gratefully acknowledge support from SC NASA EPSCoR RGP 2024 and NASA under award No 80NSSC24K0900. DAB acknowledges support from IIT-Indore, through a Young Faculty Research Seed Grant (project: 'INSIGHT'; IITI/YFRSG/2024-25/Phase-VII/02).

Software: Cosmos++ (Anninos et al. 2005); Pandurata (Schnittman & Krolik 2013)

REFERENCES

- Begelman, M. C., & Armitage, P. J. 2014, ApJL, 782, L18, doi: 10.1088/2041-8205/782/2/L18
- Belloni, T. M. 2010, in Lecture Notes in Physics, Berlin Springer Verlag, ed. T. Belloni, Vol. 794, 53, doi: 10.1007/978-3-540-76937-8-3
- Bollimpalli, D. A., Fragile, P. C., Dewberry, J. W., & Kluźniak, W. 2024, MNRAS, 528, 1142, doi: 10.1093/mnras/stad3975
- Bollimpalli, D. A., Fragile, P. C., & Kluźniak, W. 2023, MNRAS, 520, L79, doi: 10.1093/mnrasl/slac155
- Chandrasekhar, S. 1960, Radiative transfer
- Cheng, Y., Liu, D., Nampalliwar, S., & Bambi, C. 2016, Classical and Quantum Gravity, 33, 125015, doi: 10.1088/0264-9381/33/12/125015
- Connors, P. A., Piran, T., & Stark, R. F. 1980, ApJ, 235, 224, doi: 10.1086/157627
- Doroshenko, V., Poutanen, J., Tsygankov, S. S., et al. 2022,
 Nature Astronomy, 6, 1433,
 doi: 10.1038/s41550-022-01799-5
- Eardley, D. M., & Lightman, A. P. 1975, ApJ, 200, 187, doi: 10.1086/153777
- Esin, A. A., McClintock, J. E., & Narayan, R. 1997, ApJ, 489, 865, doi: 10.1086/304829
- Farinelli, R., Fabiani, S., Poutanen, J., et al. 2023, MNRAS, 519, 3681, doi: 10.1093/mnras/stac3726
- Fender, R. P., Belloni, T. M., & Gallo, E. 2004, MNRAS, 355, 1105, doi: 10.1111/j.1365-2966.2004.08384.x
- Fragile, P. C., & Blaes, O. M. 2008, ApJ, 687, 757, doi: 10.1086/591936
- Fragile, P. C., Gillespie, A., Monahan, T., Rodriguez, M., & Anninos, P. 2012, ApJS, 201, 9, doi: 10.1088/0067-0049/201/2/9
- Fragile, P. C., Olejar, A., & Anninos, P. 2014, ApJ, 796, 22, doi: 10.1088/0004-637X/796/1/22
- Fragile, P. C., Straub, O., & Blaes, O. 2016, MNRAS, 461, 1356, doi: 10.1093/mnras/stw1428
- Generozov, A., Blaes, O., Fragile, P. C., & Henisey, K. B. 2014, ApJ, 780, 81, doi: 10.1088/0004-637X/780/1/81
- Gianolli, V. E., Kim, D. E., Bianchi, S., et al. 2023, MNRAS, 523, 4468, doi: 10.1093/mnras/stad1697
- Gianolli, V. E., Bianchi, S., Kammoun, E., et al. 2024, A&A, 691, A29, doi: 10.1051/0004-6361/202451645
- Ingram, A., & Done, C. 2011, MNRAS, 415, 2323, doi: 10.1111/j.1365-2966.2011.18860.x
- Ingram, A., Done, C., & Fragile, P. C. 2009, MNRAS, 397, L101, doi: 10.1111/j.1745-3933.2009.00693.x
- Ingram, A., Maccarone, T. J., Poutanen, J., & Krawczynski,
 H. 2015, ApJ, 807, 53, doi: 10.1088/0004-637X/807/1/53

- Ingram, A., van der Klis, M., Middleton, M., et al. 2016, MNRAS, 461, 1967, doi: 10.1093/mnras/stw1245
- Krawczynski, H., Muleri, F., Dovčiak, M., et al. 2022, Science, 378, 650, doi: 10.1126/science.add5399
- Kubota, A., Done, C., Tsurumi, K., & Mizukawa, R. 2024, MNRAS, 528, 1668, doi: 10.1093/mnras/stae067
- Liu, B. F., Taam, R. E., Meyer-Hofmeister, E., & Meyer, F. 2007, ApJ, 671, 695, doi: 10.1086/522619
- Marinucci, A., Muleri, F., Dovciak, M., et al. 2022, MNRAS, 516, 5907, doi: 10.1093/mnras/stac2634
- McClintock, J. E., & Remillard, R. A. 2006, in Compact stellar X-ray sources, ed. W. H. G. Lewin & M. van der Klis, Vol. 39, 157–213, doi: 10.48550/arXiv.astro-ph/0306213
- McKinney, J. C. 2006, MNRAS, 368, 1561, doi: 10.1111/j.1365-2966.2006.10256.x
- Miller, J. M., & Homan, J. 2005, ApJL, 618, L107, doi: 10.1086/427775
- Motta, S., Homan, J., Muñoz Darias, T., et al. 2012, MNRAS, 427, 595, doi: 10.1111/j.1365-2966.2012.22037.x
- Motta, S. E. 2016, Astronomische Nachrichten, 337, 398, doi: 10.1002/asna.201612320
- Motta, S. E., Casella, P., Henze, M., et al. 2015, MNRAS, 447, 2059, doi: 10.1093/mnras/stu2579
- Novikov, I. D., & Thorne, K. S. 1973, in Black Holes (Les Astres Occlus), ed. C. Dewitt & B. S. Dewitt, 343–450
- Papaloizou, J. C. B., & Pringle, J. E. 1984, MNRAS, 208, 721, doi: 10.1093/mnras/208.4.721
- Paul, B. 2022, in 44th COSPAR Scientific Assembly. Held 16-24 July, Vol. 44, 1853
- Podgorný, J., Marra, L., Muleri, F., et al. 2023, MNRAS, 526, 5964, doi: 10.1093/mnras/stad3103
- Remillard, R. A., & McClintock, J. E. 2006, ARA&A, 44, 49, doi: 10.1146/annurev.astro.44.051905.092532
- Schnittman, J. D., & Bertschinger, E. 2004, ApJ, 606, 1098, doi: 10.1086/383180
- Schnittman, J. D., Homan, J., & Miller, J. M. 2006a, ApJ, 642, 420, doi: 10.1086/500923
- Schnittman, J. D., & Krolik, J. H. 2009, ApJ, 701, 1175, doi: 10.1088/0004-637X/701/2/1175
- —. 2010, ApJ, 712, 908, doi: 10.1088/0004-637X/712/2/908
- —. 2013, ApJ, 777, 11, doi: 10.1088/0004-637X/777/1/11
- Schnittman, J. D., Krolik, J. H., & Hawley, J. F. 2006b, ApJ, 651, 1031, doi: 10.1086/507421
- van den Eijnden, J., Ingram, A., Uttley, P., et al. 2017, MNRAS, 464, 2643, doi: 10.1093/mnras/stw2634
- Veledina, A., Poutanen, J., & Ingram, A. 2013, ApJ, 778, 165, doi: 10.1088/0004-637X/778/2/165
- Weisskopf, M. C., Soffitta, P., Baldini, L., et al. 2022, Journal of Astronomical Telescopes, Instruments, and Systems, 8, 026002, doi: 10.1117/1.JATIS.8.2.026002